batteries

MDPI

*Article*

# $Bi_2Se_3$ Nanostructured Thin Films as Perspective Anodes for Aqueous Rechargeable Lithium-Ion Batteries

**Vitalijs Lazarenko [1], Yelyzaveta Rublova [1], Raimonds Meija [1], Jana Andzane [1], Vanda Voikiva [1], Artis Kons [1], Anatolijs Sarakovskis [2], Arturs Viksna [3,*] and Donats Erts [1,3,*]**

[1] Institute of Chemical Physics, University of Latvia, Raina Blvd. 19, LV-1586 Riga, Latvia
[2] Institute of Solid State Physics, University of Latvia, Kengaraga Street 8, LV-1063 Riga, Latvia
[3] Faculty of Chemistry, University of Latvia, Raina Blvd. 19, LV-1586 Riga, Latvia
* Correspondence: arturs.viksna@lu.lv (A.V.); donats.erts@lu.lv (D.E.); Tel.: +371-26400965 (A.V.); +371-67033936 (D.E.)

**Abstract:** In recent years, aqueous rechargeable lithium-ion batteries (ARLIBs) have attracted attention as an alternative technology for electrical storage. One of the perspective battery anode materials for application in ARLIBs is $Bi_2Se_3$, which has already shown good perspectives in the application of conventional lithium-ion batteries (LIBs) that use organic electrolytes. In this study, the electrochemical properties of $Bi_2Se_3$ thin films with two different layers on the electrode surface—the solid electrolyte interphase (SEI) and the $Bi_2O_3$ layer—were investigated. The results of this work show that the formation of the SEI layer on the surface of $Bi_2Se_3$ thin films ensures high diffusivity of $Li^+$, high electrochemical stability, and high capacity up to 100 cycles, demonstrating the perspectives of $Bi_2Se_3$ as anode material for ARLIBs.

**Keywords:** bismuth selenide ($Bi_2Se_3$); anode; aqueous rechargeable lithium-ion batteries (ARLIBs); solid electrolyte interphase (SEI); bismuth oxide ($Bi_2O_3$); electrochemical performance



**Citation:** Lazarenko, V.; Rublova, Y.; Meija, R.; Andzane, J.; Voikiva, V.; Kons, A.; Sarakovskis, A.; Viksna, A.; Erts, D. $Bi_2Se_3$ Nanostructured Thin Films as Perspective Anodes for Aqueous Rechargeable Lithium-Ion Batteries. *Batteries* **2022**, *8*, 144. https://doi.org/10.3390/batteries8100144

Academic Editor: King Jet Tseng

Received: 28 July 2022
Accepted: 21 September 2022
Published: 25 September 2022



## 1. Introduction

LIBs have dominated the field of battery technology in the last few decades due to their remarkable advantages such as high energy density (>200 Wh $kg^{-1}$), high Coulombic efficiency (>95%), and long cycle life (3000 cycles at the deep discharge of 20%) [1–3]. The disadvantages of lithium-ion batteries include the flammability of non-aqueous solvents (e.g., ethylene carbonate, dimethyl carbonate, etc.), which may lead to accidents, and the high costs of fabrication (the average LIB cell cost in 2021 was EUR 104/kWh) [4]. Alternatively, in 1994, Dahn's group proposed aqueous rechargeable lithium-ion batteries (ARLIBs) consisting of $LiMn_2O_4/VO_2$ in the 5 M $LiNO_3$ electrolyte [5]. This battery demonstrated an average voltage of 1.5 V with an energy density of 75 Wh $kg^{-1}$, which was higher than the energy density of Pb-acid batteries (30 Wh $kg^{-1}$) [5].

For a long time, investigations on the development of aqua-based batteries were suspended due to several serious limitations—poor cycling performance, low voltage potential window (1.23 V), and decomposition of the water, which made these batteries commercially unviable [6]. In the last 5 years, the requirement for cheap, safe, and environmentally friendly energy storage devices has generated a great deal of interest. ARLIBs have been shown to be one of the potential candidates for the most suitable battery systems to meet these requirements. Thus, the interest in research into this battery technology has only increased [7]. Such a rapid development might allow for the production of ARLIBs with properties that are competitive in the worldwide market [8].

While significant progress has been achieved in the development of cathode materials (e.g., enhancement of mechanical stability), the research on anode materials has been limited [9]. Among a variety of material candidates for the ARLIBs anodes (e.g., $Li_{1.2}V_3O_8$, $VO_2$, $TiP_2O_7$) [10–12], the $TiP_2O_7$ is considered to be the most promising [10,13]; however,

it suffers significant capacity fading during charge/discharge processes, which might be related to the deterioration of the anode material [11].

Another possible perspective anode material for ARLIBs comes from bismuth chalcogenides $Bi_2X_3$ (X = S, Te, Se), which are unique lamellar materials with high ionic conductivity that have shown great performance in organic electrolyte LIBs [12]. Among the chalcogenides, $Bi_2Se_3$ has the highest density and theoretical volumetric capacity (3667 mAh $cm^{-3}$) [14], which, being coupled with its high electrical conductivity (10.6 S $cm^{-1}$ at 300 K) [15], allows for the possibility of fabricating compact electrical devices [14,16].

The crystal lattice of $Bi_2Se_3$ consists of a sequential layer arrangement that is perpendicular to the trigonal C-axis [17]. Each molecule consists of five atomic planes arranged in the following pattern: $Se^1$-Bi-$Se^2$-Bi-$Se^1$, where van der Waals gaps are located between $Se^1$ atoms [18]. The thickness of such a quintuple layer is about 1 nm. The arrangement of quintuple layers provides enough space for $Li^+$ during intercalation and deintercalation processes, which makes them suitable anode materials for LIBs [19].

While both $Bi_2Se_3$ and $TiP_2O_7$ have higher potential for $Li^+$ intercalation than for $H_2$ evolution, which allows for avoiding unwanted side reactions [20], $Bi_2Se_3$ is still considered a more unique material due to its quintuple layer structure. $Bi_2Se_3$ has a ~4 times higher theoretical gravimetric capacity than $TiP_2O_7$ (491 mAh $g^{-1}$ [12] vs. 121 mAh $g^{-1}$ [21]).

Additionally, in anode material research, special attention should be paid to the formation of the solid-electrolyte interphase (SEI) layer, which impacts the safety and stability of the anode electrode [22]. In aqueous electrolytes, the SEI layer consists of two layers: $Li_2O$ (inner layer) and $Li_2CO_3$ (outer layer), which are formed by $Li^+$ reactions with dissolved $O_2$ and $CO_2$ [23–27]. For the ARLIBs, it is necessary to use concentrated aqueous electrolytes, which will ensure the formation of stable SEI layers as, in the diluted electrolytes, the SEI layer quickly undergoes hydrolysis and dissolves [25,27].

In this work, the electrochemical properties of $Bi_2Se_3$ thin films are investigated for the first time to evaluate their possible application as anode electrodes in ARLIBs. To examine the formation of the SEI layer and its effect on the performance of the $Bi_2Se_3$ anode, measurements were carried out in two different potential ranges. One of the potential ranges ensured the formation of the SEI layer on the surface of $Bi_2Se_3$, and the other did not. 5 M $LiNO_3$ solution, which is electrochemically more stable than LiCl and $Li_2SO_4$ [28] and can be prepared in high concentrations (up to 9 M) [6], was used as an electrolyte.

## 2. Material and methods

### *2.1. Synthesis and Characterization of $Bi_2Se_3$*

$Bi_2Se_3$ thin films were synthesized on microscope glass slides (25 × 75 mm) using the physical vapor deposition method [29–31]. The synthesis procedure was performed in a programmable quartz tube (length = 60 cm, diameter = 4.5 cm) furnace *(GSL-1100x-S, MTI Corp.)* with adjustable valves on both sides.

In total, 15 mg of raw $Bi_2Se_3$ (Sigma-Aldrich, Burlington, MA, USA, *99.999%*) was weighted in ceramic boats using analytical scales *(KERN "ABP 200-5DM", ±0.01 mg*, Balingen, Germany). Inside the quartz tube at certain temperature regions, microscope glass slides (330–380 °C) and raw $Bi_2Se_3$ (585 °C) were inserted. The quartz tube was connected to the $N_2$ gas cylinder (Linde, Berlin, Germany, *99.999%*) and a vacuum pump. Before the synthesis, the quartz tube was purged with $N_2$ and vacuumed. The synthesis of $Bi_2Se_3$ thin films was performed according to the following protocol: first, linear heating of the quartz tube for 45 min up to a temperature of 585 °C; second, maintaining a constant temperature for 15 min (pressure 2–3 Torr); and third, gradual cooling down to 470 °C, reinjecting $N_2$ gas into the tube up to atmospheric pressure, and cooling down to room temperature.

The morphology and stoichiometry of the samples were investigated with a scanning electron microscope (SEM) (*Hitachi FE-SEM S-4800*, Marunouchi, Tokyo, Japan) equipped with an energy-dispersive X-ray (EDX) (*Bruker XFLASH 5010*, Billerica, MA, USA) detector, X-ray diffraction analysis (XRD) (*Bruker D8 Discover*, Billerica, MA, USA), and X-ray

photoelectron spectroscopy (XPS) (*ThermoFisher Escalab 250Xi*$^+$, Walthman, MA, USA) with monochromatic Al-K$_\alpha$ X-ray source).

### *2.2. Electrochemical Measurements*

The electrochemical measurements were performed at room temperature using a 3-electrode cell with 3 M Ag/AgCl as a reference electrode (RE), Pt wire as a counter electrode (CE)—(ItalSens, PalmSens, Houten, The Netherlands), and $Bi_2Se_3$ thin film on the glass substrate as a working electrode (WE)—(Supplementary Figure S1). 5 M $LiNO_3$ (ThermoFisher, Walthman, MA, USA, *analytical grade 99%*) was used as an electrolyte. To ensure appropriate electrical contact, copper wire was fixed to the surface of the working electrode with silver conductive paint (Electrolube, Ashby-de-la-Zouch, UK). Cyclic voltammetry (CV), electrochemical impedance spectroscopy (EIS), and galvanostatic charge/discharge measurements were performed by potentiostat PalmSens4. CV curves were measured at different scan rates (0.1–1.0 mV s$^{-1}$). The galvanostatic charge/discharge measurements were carried out at room temperature with a C-rate of 1 C. EIS spectra were measured in the frequency range of 0.01–10000 Hz at open circuit potential before and between the galvanostatic charge/discharge cycles (after the 1st, 2nd, 5th, 50th, and 100th cycle). After CV measurements, the $Bi_2Se_3$ samples were washed ~4–5 times with deionized water, dried, and investigated using the SEM, EDX, and XPS analysis methods.

## 3. Results and Discussion

### *3.1. Characterization of Synthesized $Bi_2Se_3$ Thin Film*

To increase the effective interaction surface between the electrode and the electrolyte, the synthesis method for $Bi_2Se_3$ thin films with nanoplates that grow at different angles (partly disordered) to the substrate surface was selected [32,33] (Figure 1a). This type of $Bi_2Se_3$ morphology has no dead volume or gap spacing shrinkage [34] which could lead to the decrease of the anode active sites, thus making it a promising candidate as anode material for ARLIBs. The size of the nanoplates varied between 1.0 and 8.0 µm. The thickness of the synthesized $Bi_2Se_3$ thin films with partly disordered nanoplates was between 350 and 500 nm. The EDX spectra (Supplementary Figure S2) showed intensive peaks of C, O, Se, Si, and Bi. Si, O, and C peaks were the background signals from the microscope glass slides on which $Bi_2Se_3$ was synthesized. The Se/Bi atomic ratio determined from the EDX spectra was 1.44 ± 0.03, which is close to the theoretical stoichiometric ratio of $Bi_2Se_3$ (1.50) and indicates a rather uniform chemical composition of the films. The XRD pattern (Figure 1b) of $Bi_2Se_3$ powder obtained by scratching the synthesized thin film off the substrate showed $Bi_2Se_3$ diffraction peaks, which refer to the rhombohedral (R-3 m) crystal system of $Bi_2Se_3$ (Ref. card No. PDF 01-085-9274): a = b = 4.13850 Å; c = 28.62400 Å, as well as cubic $\gamma$-$Bi_2O_3$ (I23) (Ref. card. No. PDF 01-074-1375) with crystal system a = b = c = 10.08000 Å. It should be noted that the difference in the peak intensity ratios between the reference cards and the actual XRD patterns obtained for the powdered $Bi_2Se_3$ thin films most likely are related to the impact of the substrate on the growth of $Bi_2Se_3$ thin films, resulting in the domination of certain crystallographic growth directions [32,33]. The formation of $Bi_2O_3$ could be explained by the oxidation of $Bi_2Se_3$ powder, which, due to its increased surface area after scratching, is more prone to oxidation in an ambient environment.

### *3.2. Electrochemical processes and mechanisms of $Bi_2Se_3$ thin film*

Cyclic voltammetry of $Bi_2Se_3$ thin films in 5 M $LiNO_3$ at the scan rate of 0.25 mV s$^{-1}$ in the potential range (−1.0 ÷ 1.3 V vs. Ag/AgCl) showed two cathodic peaks (I, II) and four anodic peaks (III, IV, V, VI) (Figure 2a). The peaks I (−0.65 V vs. Ag/AgCl) and III (0.02 V vs. Ag/AgCl) represent the intercalation/deintercalation processes of $Li^+$ according to the reaction in Equation (1) [19]. The peaks II (−0.71 V vs. Ag/AgCl) and IV (−0.65 V vs. Ag/AgCl) are related to the substitution reaction of $Bi_2Se_3$ and $Li_2Se$ (Equation (2)) [18,35]. Anodic peak V (0.61 V vs. Ag/AgCl) might describe a

formation of $NO_2^-$ from $NO_3^-$ (Equation (3)) [36]. $NO_2^-$ can be rapidly oxidized back to $NO_3^-$ due to the presence of dissolved $O_2$ in the electrolyte [37]. The peak VI (0.84 V vs. Ag/AgCl) appeared only in the first cycle and was attributed to the formation of the SEI layer, which, according to the literature on the other aqueous $Li^+$ systems ($Mo_6S_8$, carbon-coated $TiO_2$, and carbon electrodes), is most probably composed of $Li_2O$ and $Li_2CO_3$ (Equations (4) and (5)) [24–26,38,39].

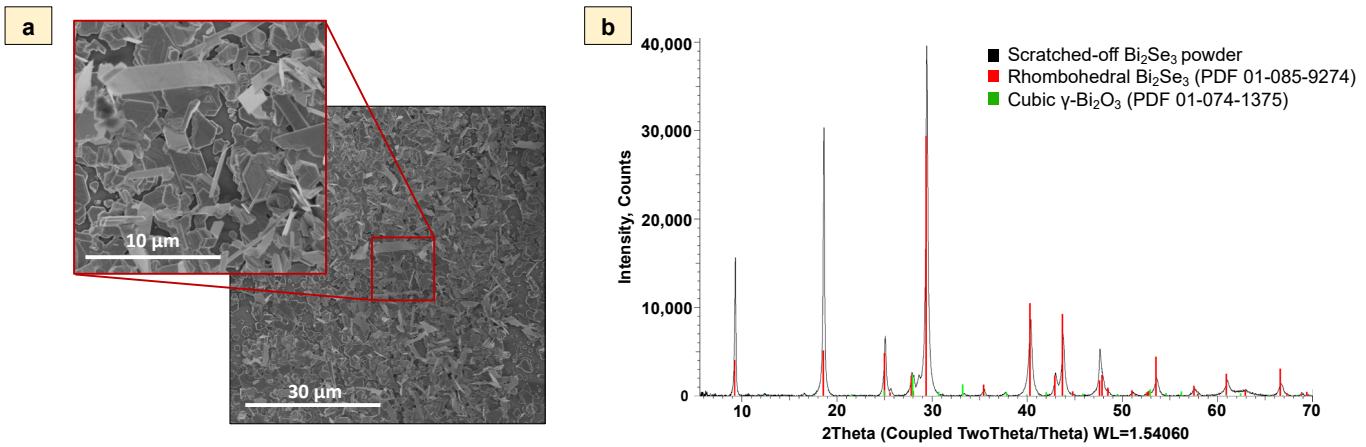


**Figure 1.** (**a**)—SEM image of $Bi_2Se_3$ thin films on the glass substrate, (**b**)—XRD pattern of $Bi_2Se_3$ powder obtained by scratching the as-grown thin film off the substrate.

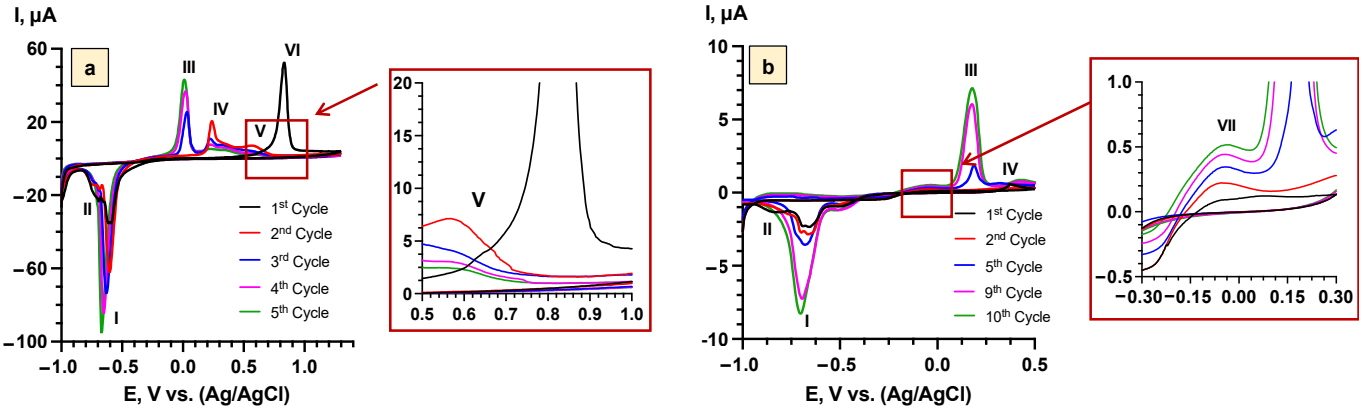


**Figure 2.** Cyclic voltammograms of $Bi_2Se_3$ thin films in 5 M $LiNO_3$ at the scan rates 0.25 mV $s^{-1}$: (**a**)—samples with SEI layer (−1.0 V ÷ 1.3 V vs. Ag/AgCl), (**b**)—samples with $Bi_2O_3$ layer (−1.0 V ÷ 0.5 V vs. Ag/AgCl).

To avoid the formation of $NO_2^-$ in the solution (at 0.61 V vs. Ag/AgCl) and to investigate the impact of the SEI layer on the stability and operation of the $Bi_2Se_3$ electrode in the aqueous electrolyte, parallel experiments were performed in the narrower potential range (−1.0 ÷ 0.5 V vs. Ag/AgCl) (Figure 2b). In this case, a new low-intensity anodic peak VII (−0.05 V vs. Ag/AgCl) appeared starting from the second cycle. This peak might be related to the formation of the $Bi_2O_3$ layer on the surface of $Bi_2Se_3$ by the reaction with dissolved oxygen in the electrolyte (Equation (6)) [40,41]. For the wide potential range (−1.0 ÷ 1.3 V vs. Ag/AgCl), this peak was not observed, which indicates that, after the formation of the SEI layer on the surface of $Bi_2Se_3$, further formation of $Bi_2O_3$ was inhibited. Further in the text, both potential ranges are referred to as "samples with the SEI layer" (−1.0 ÷ 1.3 V vs. Ag/AgCl) and "samples with the $Bi_2O_3$ layer" (−1.0 ÷ 0.5 V vs. Ag/AgCl).

It is important to note that the CV peak potential values obtained in this work may differ from the values reported in the literature by 0.6–1.0 V in terms of the standard

hydrogen potential scale. This is due to the fact that, in this work, the 3-electrode cell configuration was used, which allowed us to measure the properties of the anode material solely, while in the literature, the 2-electrode cell configuration was applied, thus measuring the properties of the whole cell.

$$Bi_2Se_3 + xLi^+ + xe^- \leftrightarrow Li^+{}_x[Bi_2Se_3]^{x-}, \quad (1)$$

$$Bi_2Se_3 + 6Li^+ + 6e^- \leftrightarrow 3Li_2Se + 2Bi, \quad (2)$$

$$NO_3{}^- + 2H^+ + 2e^- \rightarrow NO_2{}^- + H_2O, \quad (3)$$

$$O_2 + 4Li^+ + 4e^- \rightarrow 2Li_2O, \quad (4)$$

$$2Li^+ + \frac{1}{2}O_2 + CO_2 + 2e^- \rightarrow Li_2CO_3, \quad (5)$$

$$4Bi^{3+} + 3O_2 + 6e^- \rightarrow 2Bi_2O_3. \quad (6)$$

For both samples with the formed SEI layer and with the $Bi_2O_3$ layer, the intensities of peaks corresponding to $Li^+$ intercalation/deintercalation processes (I, III) in subsequent cycles increased (Figure 2a,b). The increase in the intensity of $Li^+$ intercalation/deintercalation processes may be related to the pre-treatment of $Bi_2Se_3$. The pre-treatment involves the stabilization of the SEI ($-1.0 \div 1.3$ V vs. Ag/AgCl) and the $Bi_2O_3$ ($-1.0 \div 0.5$ V vs. Ag/AgCl) layers until their continuous coverage of the entire electrode's surface.

Charge/discharge curves obtained for the $Bi_2Se_3$ thin films in the potential range ($-1.0 \div 1.3$ V vs. Ag/AgCl) at the C-rate 1C (Figure 3a) exhibited, in the first cycle, a plateau near 0.6 V. This confirmed the formation of the SEI layer. In the next cycles, this plateau was not observed, which confirms that the layer formation process was finished. These findings are in line with the data reported by the other groups, pointing out that the fully developed SEI layer, which is stable and ensures long-term capacity retention and high Coulombic efficiency, forms in the first cycle due to an irreversible electrochemical reaction [42]. In the subsequent cycles, charge ($-0.55$ V) and discharge ($-0.02$ V) plateaus, corresponding to $Li^+$ intercalation and deintercalation, respectively, were observed (Figure 3a). Although the SEI layer was formed in the first cycle, the charge/discharge profiles were changing until the third cycle (samples with the SEI layer), indicating that, during the first three cycles, the surface pre-treatment took place. After the pre-treatment of the $Bi_2Se_3$, the charge/discharge profiles did not change significantly (Figure 3a).

Additionally, the voltammograms (Figure 2a) showed that after the formation of the SEI layer in the first cycle, the peaks corresponding to the processes of $Li^+$ intercalation/deintercalation slightly shifted towards the negative potential, which might be related to the structural and textural modification of $Bi_2Se_3$ [43]. A similar tendency was also observed for the anodic peak (V) associated with $NO_2{}^-$ formation, where, after the first cycle, the peak had shifted from 0.67 V to 0.61 V vs. Ag/AgCl (Figure 2a).

For the samples with the $Bi_2O_3$ layer, the plateau corresponding to the intercalation process was observed already in the first cycle, while the plateau corresponding to the deintercalation process was observed starting with the second cycle (Figure 3b), as there were no $Li^+$ ions intercalated into $Bi_2Se_3$ at the beginning of the first anodic (discharge) scan from $-1$ V to 6 + 0.5 V vs. Ag/AgCl. The change in the charge/discharge profiles was observed up to the ninth cycle (Figure 3b), indicating slower pre-treatment of the $Bi_2Se_3$ surface in comparison to the samples with the SEI layer, as well as the formation of the $Bi_2O_3$ layer.

After pre-treatment, the formed SEI or $Bi_2O_3$ layers on the surfaces of the $Bi_2Se_3$ electrodes inhibited further substitution reaction (Equation (2)), which is characterized by decreased peak intensities (II, IV).

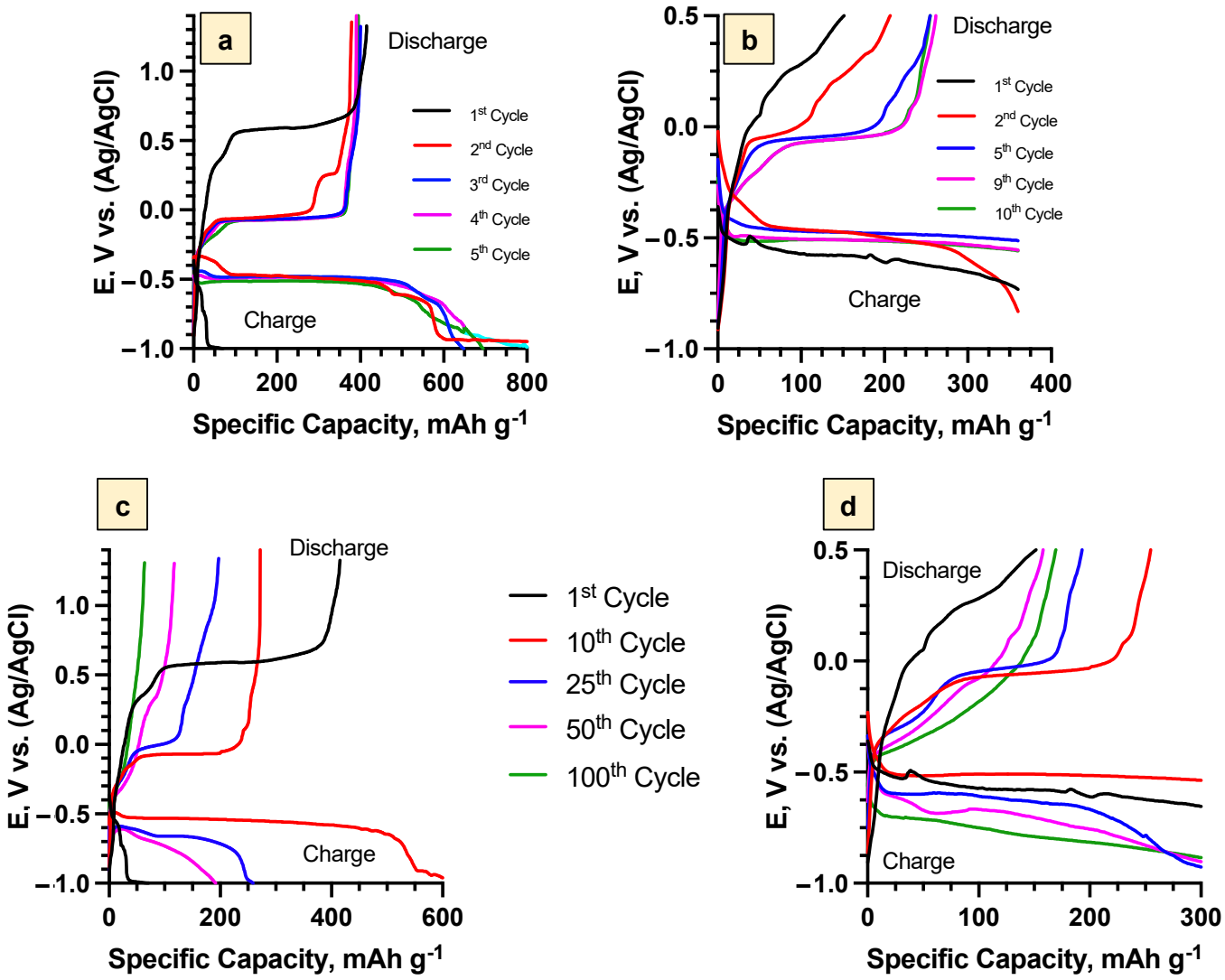


**Figure 3.** Charge/Discharge profiles of $Bi_2Se_3$ thin films in 5 M $LiNO_3$ at 1 C: (**a**)—first 5 cycles for the SEI layer (−1.0 V ÷ 1.3 V), (**b**)—first 10 cycles for the $Bi_2O_3$ layer (−1.0 V ÷ 0.5 V), (**c**)—profiles up to the 100th cycle for the SEI layer (−1.0 V ÷ 1.3 V), (**d**)—profiles up to the 100th cycle for the $Bi_2O_3$ layer (−1.0 V ÷ 0.5 V).

The comparison of the heights of the peaks corresponding to $Li^+$ intercalation/deintercalation (I, III) showed that they were up to 10 times higher for the samples with formed SEI layers than for the samples with formed $Bi_2O_3$ layers, which could have been related to the higher transportation rate of $Li^+$ in the samples with the SEI layer. This may mean that, while $Bi_2O_3$ has been shown as a suitable additive in $Bi_2Se_3$ water-based battery systems [44], its performance as an "SEI" layer is not optimal as its high density inhibits ion transport.

SEM images and XRD patterns acquired from the samples' surface XPS spectra demonstrated the structural differences of the $Bi_2Se_3$ thin film surface before and after 5 cycles and 10 cycles for the samples covered with continuous SEI and $Bi_2O_3$ layers, respectively (Figures 4 and 5).

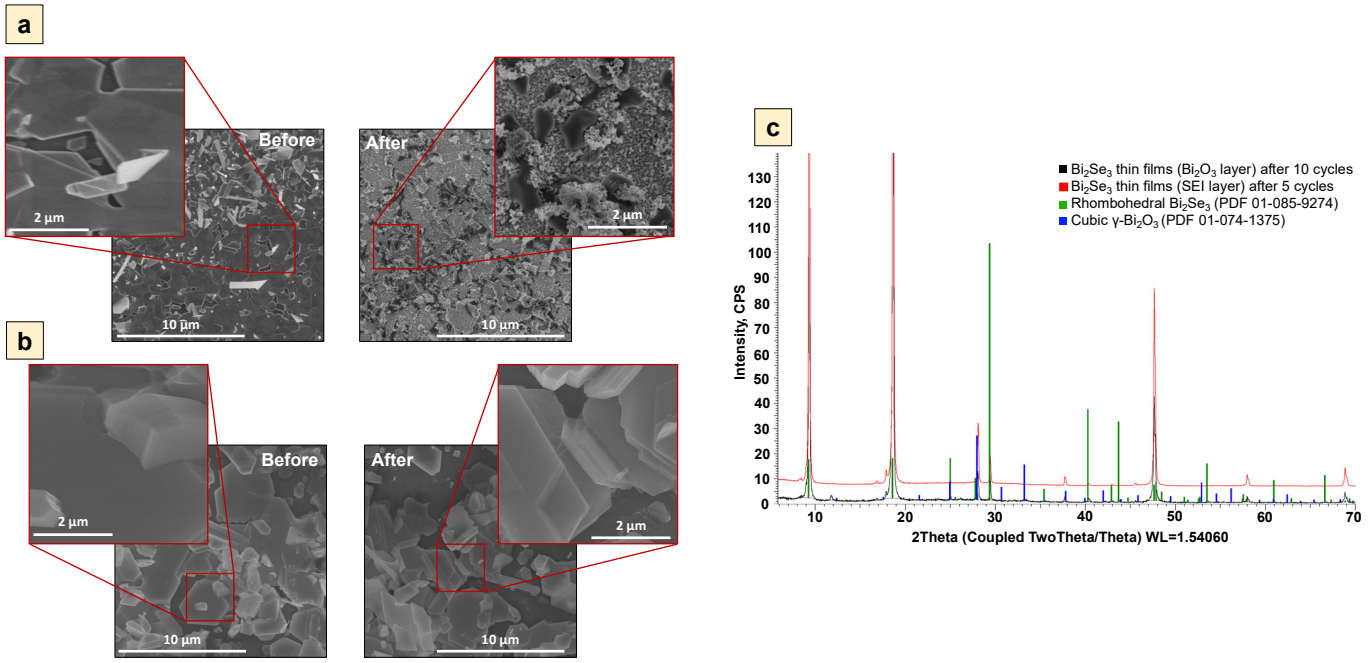


**Figure 4.** Scanning electron microscope images of $Bi_2Se_3$ thin films in 5 M $LiNO_3$ before and after cyclic voltammetry measurements for: (**a**)—SEI layer after 5 cycles (−1.0 V ÷ 1.3 V), (**b**)—$Bi_2O_3$ layer after 10 cycles (−1.0 V ÷ 0.5 V), (**c**)—XRD pattern of samples with *SEI layer* after 5 cycles (−1.0 V ÷ 1.3 V) and $Bi_2O_3$ layer after 10 cycles (−1.0 V ÷ 0.5 V).

According to the observation by SEM, the surface of the sample with the SEI layer after five cycles was coated with amorphous material (Figure 4a). The XPS data (Figure 5a) showed a noticeable Li 1s peak, which may indicate the presence of $Li_2O$ and $Li_2CO_3$. The water-soluble $Li_2O$ could have been preserved if the $Li_2CO_3$ had grown on top of it and had shielded it from the electrolyte (Equations (4) and (5)). While the XRD pattern of the sample with the SEI layer demonstrated pure rhombohedral $Bi_2Se_3$ (R-3 m) without the initial cubic y-$Bi_2O_3$ signal (Figure 4c), the XPS data still showed a $Bi_2O_3$ signal (Figure 5b). This indicates that the initial $Bi_2O_3$ has remained, but further growth of the $Bi_2O_3$ was inhibited by the formation of the SEI layer.

In turn, the sample with the $Bi_2O_3$ layer after 10 cycles had a smooth surface (Figure 4b), which could mean that the $Bi_2Se_3$ thin film was covered with the thin and dense $Bi_2O_3$ layer. This assumption is supported by both XRD and XPS data where a small cubic $\gamma$-$Bi_2O_3$ (I23) peak (Figure 4c) and very pronounced peaks related to the oxidized Bi (Bi 4f, Figure 5d) were detected. It should be noted that only a very small peak of $Bi_2Se_3$ is observed in the surface layer of the sample (Figure 5c), which confirms that it is mainly composed of $Bi_2O_3$ and proves the formation of continuous dense layers of $Bi_2O_3$. In addition, the representing SEI layer Li 1s peak is negligible for the samples coated with the $Bi_2O_3$ layer (Figure 5c), which proves the absence of SEI layers composed of $Li_2O$ and $Li_2CO_3$ on the surface of these samples.

These data support the claim that, during cycling in the potential window (−1.0 ÷ 0.5 V), the dense $Bi_2O_3$ layer is formed, and this layer may inhibit $Li^+$ intercalation/deintercalation processes, which results in the decrease of the heights of the CV peaks for the samples coated with the $Bi_2O_3$ layer (Figure 2).

The stability of $Bi_2Se_3$ thin films in terms of the chemical composition of Bi and Se was checked with EDX before cycling and after the fifth (sample with the SEI layer) and ninth (sample with the $Bi_2O_3$ layer) cycles. While it is well known that $Bi_2Se_3$ tends to lose selenium during the cycling [15], the results of this study demonstrate that the dissolution of Se for both samples covered with SEI and $Bi_2O_3$ layers was negligible (Table 1), which

indicates the good stability of the $Bi_2Se_3$ electrode in the $LiNO_3$ for the first 5 (SEI layer) and 10 ($Bi_2O_3$ layer) cycles.

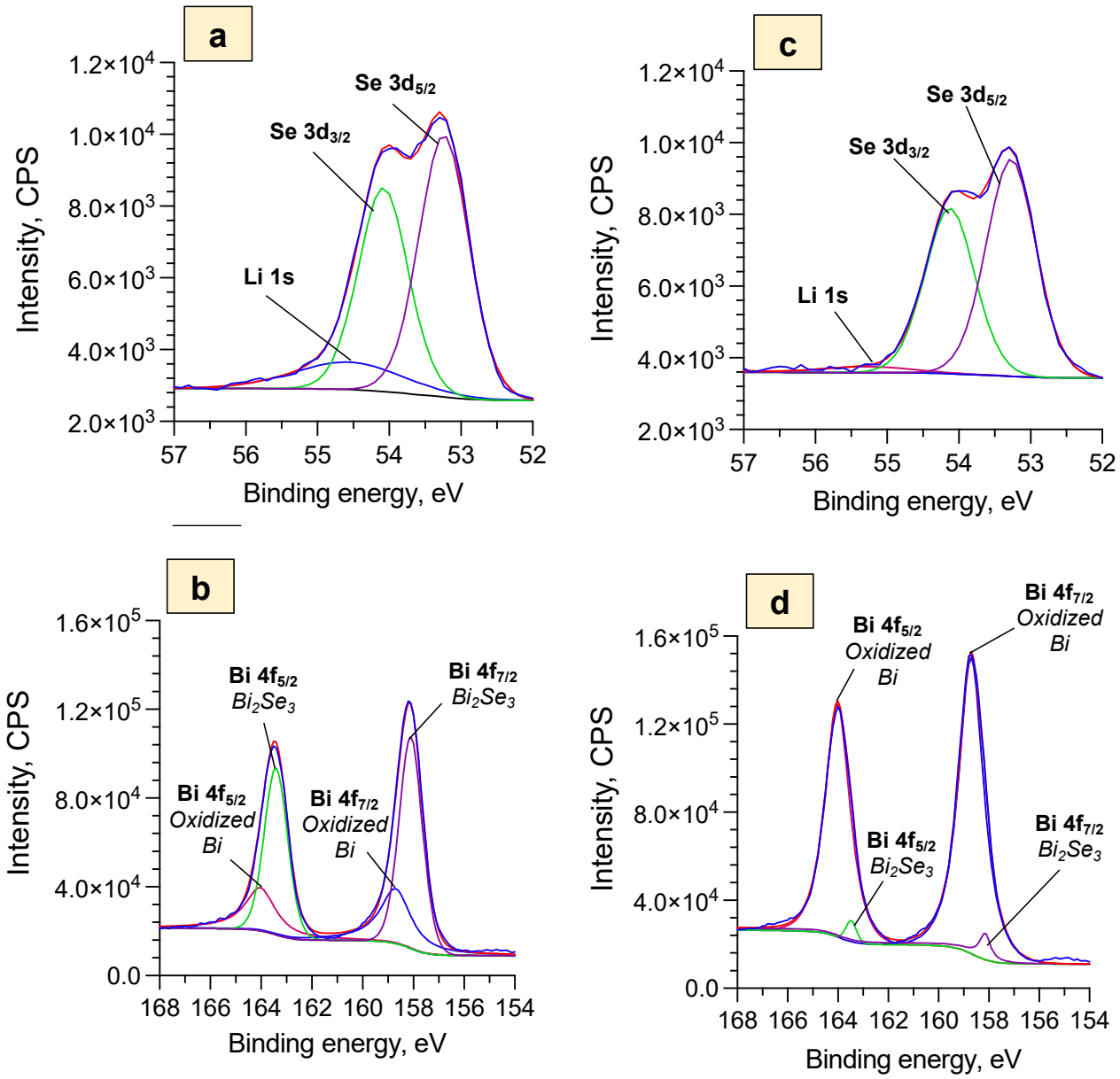


**Figure 5.** XPS spectra of $Bi_2Se_3$ thin films in 5 M $LiNO_3$ after cyclic voltammetry measurements for: (**a**)—SEI layer Se 3d and Li 1s data after 5 cycles (−1.0 V ÷ 1.3 V), (**b**)—SEI layer Bi 4f data after 5 cycles (−1.0 V ÷ 1.3 V), (**c**)—$Bi_2O_3$ layer Se 3f and Li 1s data after 10 cycles (−1.0 V ÷ 0.5 V), (**d**)—$Bi_2O_3$ layer Bi 4f data after 10 cycles (−1.0 V ÷ 0.5 V).

**Table 1.** The atomic composition of $Bi_2Se_3$ thin films in 5 M $LiNO_3$ before and after CV measurements.

| Element | Before | After 5 Cycles (SEI Layer) | After 10 Cycles ($Bi_2O_3$ Layer) |
|---|---|---|---|
| Bi | 41 ± 1 | 46 ± 3 | 41 ± 1 |
| Se | 59 ± 1 | 54 ± 3 | 59 ± 1 |

Charge/discharge profiles up to 100 cycles for the samples with the SEI and $Bi_2O_3$ layers demonstrated $Li^+$ intercalation/deintercalation plateaus from the 5th to 25th cycle

(Figure 3c,d). After the 25th cycle, these plateaus were not observable anymore, which might be due to the fast process of $Li^+$ intercalation/deintercalation [45].

To investigate the mechanisms of $Li^+$ intercalation/deintercalation processes in the $Bi_2Se_3$ thin film, the CV curves were obtained at different scan rates (0.1–1.0 mV $s^{-1}$) after the surface pre-treatment was finished (the third cycle for the samples with SEI layer (Figure 6a) and ninth cycle for the samples with $Bi_2O_3$ (Figure 6b)).

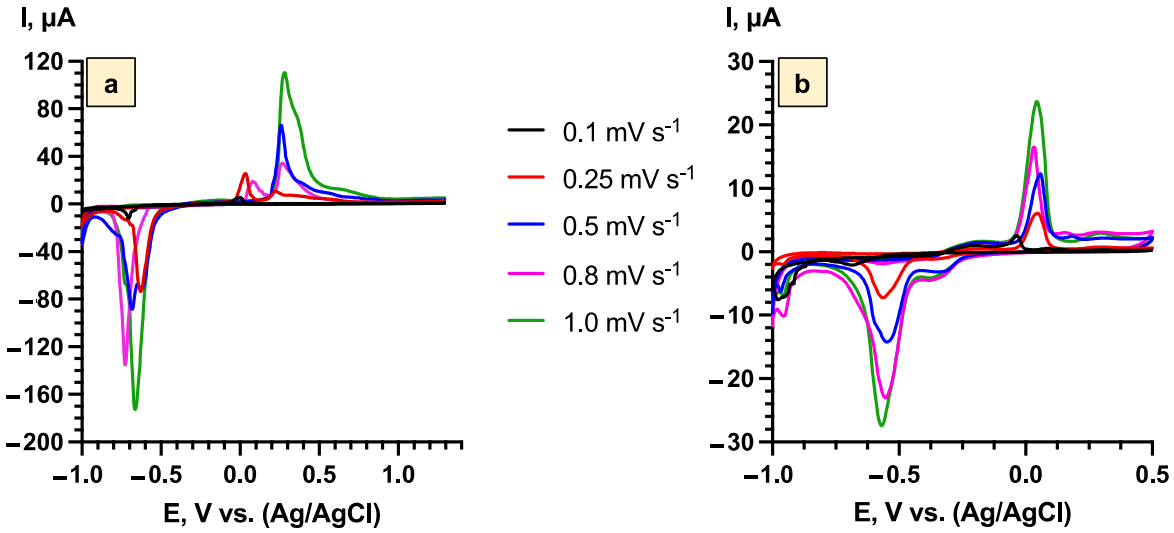


**Figure 6.** Cyclic voltammetry curves of $Bi_2Se_3$ thin films in 5 M $LiNO_3$ in the scan rate range from 0.1 to 1.0 mV $s^{-1}$ after surface pre-treatment for: (**a**)—SEI layer after third cycle (−1.0 V ÷ 1.3 V vs. Ag/AgCl), (**b**)—$Bi_2O_3$ layer after ninth cycle (−1.0 V ÷ 0.5 V vs. Ag/AgCl).

The dominant stage of $Li^+$ intercalation/deintercalation processes (diffusion-controlled or capacitive process) was determined by Equation (7) [46]:

$$I = av^b, \tag{7}$$

where $I$ is the current of the $Li^+$ intercalation/deintercalation process (mA), $v$ is the scan rate (mV $s^{-1}$), and $a$, $b$ are the adjustable fitting values.

Calculated from the linear regression slopes (Figure 7a,b), the b-values for both samples with SEI and $Bi_2O_3$ layers varied from 1.05 to 1.28, indicating the dominant contribution of the capacitive process (pseudo-capacitance and electrical double-layer capacitance) to the $Li^+$ intercalation/deintercalation in both potential ranges. The quantitative contribution of the capacitive and diffusion-based processes in $Li^+$ intercalation/deintercalation at different scan rates (Figure 7c,d) was determined by Equation (8):

$$i(V) = k_1 v + k_2 v^{\frac{1}{2}}, \tag{8}$$

where $i(V)$ is the current of the $Li^+$ intercalation/deintercalation process, $k_1 v$ is the contribution of the capacitive process, and $k_2 v^{1/2}$ is the contribution of the diffusion-controlled process [47,48].

At the scan rate of 0.1 mV $s^{-1}$, the contribution of the capacitive process to $Li^+$ intercalation/deintercalation was similar (51.4% and 53.9%) for the samples with SEI and $Bi_2O_3$ layers, respectively (Figure 7c,d). With the increasing scan rate, the contribution of the capacitive process increased, and at the scan rate of 1.0 mV $s^{-1}$, it reached 78.3% for the samples with the SEI layer and 75.4% for the samples with the $Bi_2O_3$ layer. The higher contribution of the capacitive processes to the $Li^+$ intercalation/deintercalation process in the scan rate range from 0.25 to 1.00 mV $s^{-1}$ indicates the removal of limitations on charge transfer processes for both SEI and $Bi_2O_3$ layers.

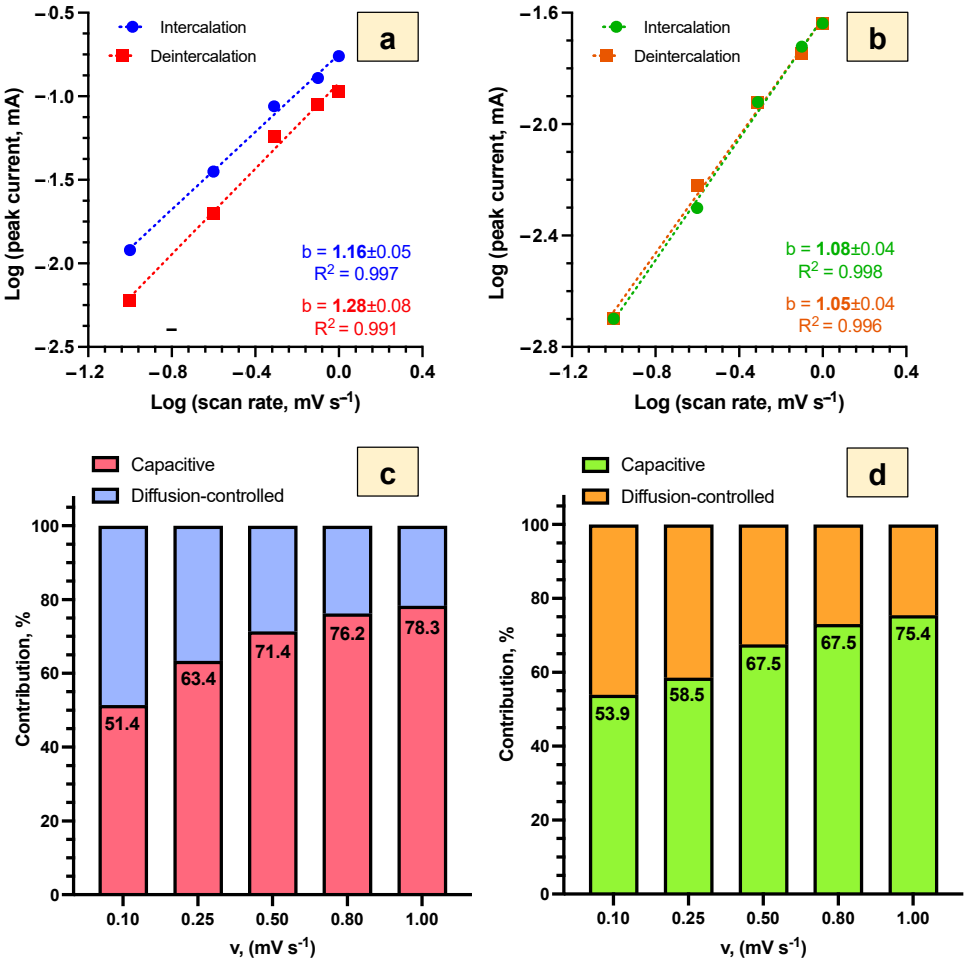


**Figure 7.** Investigation of the dominant stage and contribution of capacitive and diffusion-based processes for $Li^+$ intercalation/deintercalation in $Bi_2Se_3$ thin films in 5 M $LiNO_3$: (**a**)—log-scale plots for the SEI layer (−1.0 V ÷ 1.3 V vs. Ag/AgCl), (**b**)—log-scale plots for the $Bi_2O_3$ layer (−1.0 V ÷ 0.5 V vs. Ag/AgCl), (**c**)—the contribution of capacitive and diffusion-controlled processes for the SEI layer (−1.0 V ÷ 1.3 V vs. Ag/AgCl), (**d**)—the contribution of capacitive and diffusion-controlled processes for the $Bi_2O_3$ layer (−1.0 V ÷ 0.5 V vs. Ag/AgCl).

As the capacitive processes of $Li^+$ intercalation/deintercalation were similar for the samples with the SEI and $Bi_2O_3$ layers, and thus could not explain the differences between them, the diffusion coefficients for $Li^+$ intercalation/deintercalation were determined. The diffusion coefficients of $Li^+$ intercalation/deintercalation were calculated from the slope fitted values (Figure 8) using Equation (9) [49]:

$$D = \left(\frac{slope}{0.446nFAC}\right)^2 \left(\frac{RT}{nF}\right), \quad (9)$$

where $D$ is the diffusion coefficient ($cm^2\ s^{-1}$), *slope* is the slope value, $n$ is the number of electrons, $F$ is the Faraday constant ($C\ mol^{-1}$), $A$ is the surface area ($cm^2$), $C$ is the electrolyte concentration ($mol\ cm^{-3}$), $R$ is the universal gas constant ($J\ K^{-1}\ mol^{-1}$), and $T$ is the temperature (K).

Calculated diffusion coefficient values (Table 2) show that, in the first approximation, $Li^+$ diffusion for samples with the SEI layer was higher than for the samples with the $Bi_2O_3$ layer by an order of magnitude.

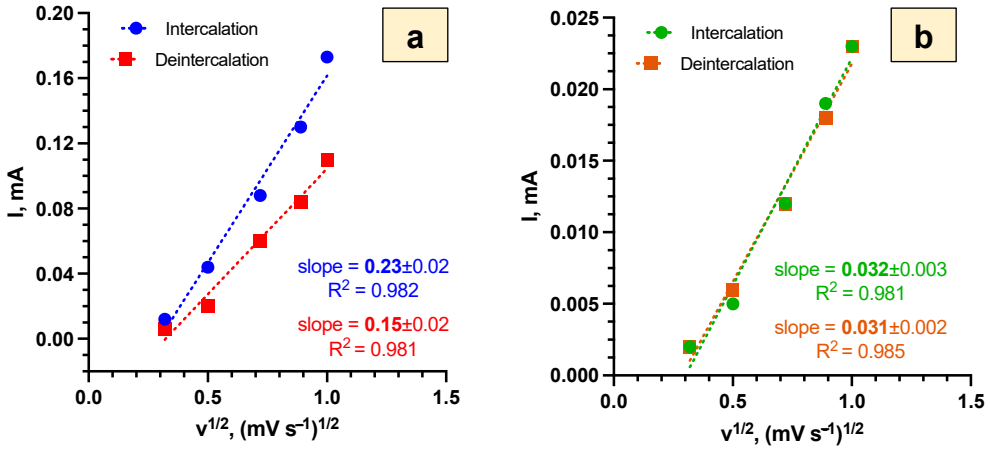


**Figure 8.** Dependence of $v^{1/2}$ vs. $I$ for $Bi_2Se_3$ thin films in 5 M $LiNO_3$ for $Li^+$ intercalation/deintercalation with fitted slope values for: (**a**)—*SEI layer* (−1.0 V ÷ 1.3 V vs. Ag/AgCl), (**b**)—*$Bi_2O_3$ layer* (−1.0 V ÷ 0.5 V vs. Ag/AgCl).

**Table 2.** Comparison of $Li^+$ intercalation and deintercalation diffusion coefficients ($cm^2$ $s^{-1}$) for different anodes and electrolytes.

| Electrode | Electrolyte | Intercalation | Deintercalation | Reference |
|---|---|---|---|---|
| $Bi_2Se_3$ thin film (SEI layer) | 5 M $LiNO_3$ | $3.3 \times 10^{-12}$ | $2.2 \times 10^{-12}$ | This study |
| $Bi_2Se_3$ thin film ($Bi_2O_3$ layer) | 5 M $LiNO_3$ | $4.3 \times 10^{-13}$ | $4.5 \times 10^{-13}$ | This study |
| $Li_{0.3}V_2O_5$ | 5 M $LiNO_3$ | $10^{-11}$–$10^{-12}$ | | [50] |
| $TiP_2O_7$ | 1 M $Li_2SO_4$ | $3.80 \times 10^{-15}$ | $1.77 \times 10^{-15}$ | [51] |
| $TiNb_6O_{17}$ | 1 M $LiPF_6$ EC/DMC [b] (1:2) | $3.43 \times 10^{-13}$ | $3.72 \times 10^{-13}$ | [52] |
| $TiNb_2O_7$ | 1 M $LiPF_6$ EC/DMC [b] (1:2) | $1.08 \times 10^{-14}$ | $3.01 \times 10^{-14}$ | |

[a] ethylene carbonate/diethyl carbonate. [b] ethylene carbonate/dimethyl carbonate.

Thus, it can be assumed that the formation of less dense $Li_2O$ and $Li_2CO_3$ SEI layers ensures the faster transportation of $Li^+$ in comparison to the $Bi_2O_3$ layer and can be the contributing factor to the difference in the peak intensities in CV curves for both samples (Figure 2).

Estimations for the $Bi_2Se_3$ thin films with SEI layer $Li^+$ diffusion coefficients were comparable with the values reported for the $Li_{0.3}V_2O_5$ in $Li^+$ aqueous electrolyte while exceeding the diffusion coefficients of $TiP_2O_7$ (1 M $Li_2SO_4$), as well as the diffusion coefficients reported for other anode materials—$TiNb_6O_{17}$ and $TiNb_2O_7$ tested in lithium non-aqueous electrolytes (Table 2). These results demonstrate that $Li^+$ diffusion coefficients for $Bi_2Se_3$ anodes in the 5 M $LiNO_3$ electrolyte are sufficient for their perspective application in ARLIBs systems.

To investigate the changes in the electrochemical properties of the $Bi_2Se_3$ thin film electrode over 100 cycles for the samples with formed SEI (Figure 9a) and $Bi_2O_3$ (Figure 9b) layers, EIS measurements were carried out. The obtained impedance hodographs were described using the standard equivalent circuit schemes, which represent the electrochemical properties at the electrolyte/electrode interface. The schemes were complicated by the presence of a constant phase element ($CPE_1$), which, in addition to the capacity of the double layer, characterized the inhomogeneity of the surface of the working electrode. The Warburg element indicated the diffusion of the reacting ions and/or molecules to the electrode surface. $R_{el}$ values demonstrated not only the resistance of the electrolyte but also the penetrability of the electrolyte within the electrode [53] (Figure 9c). During the cycling, the SEI layer for the first sample and the $Bi_2O_3$ layer for the second sample

were modeled as a capacitor formed by a CPE (characterizing the heterogeneity and the double-layer capacitance of the layer), with a parallel resistance for the charge transfer reaction (Figure 9d).

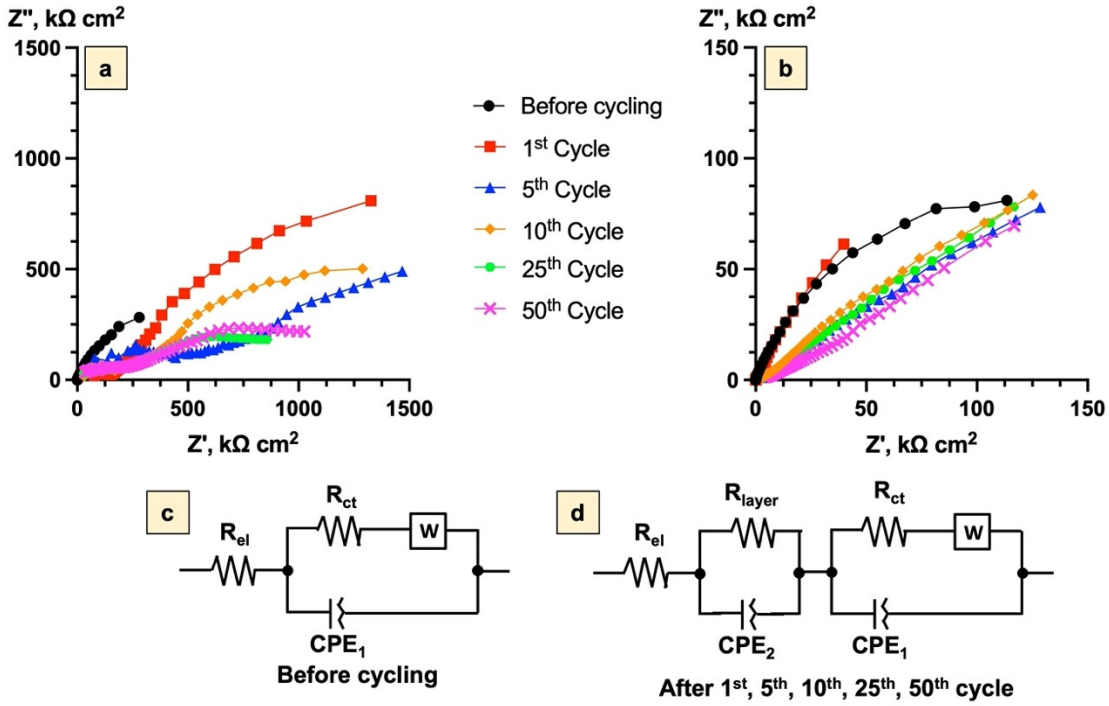


**Figure 9.** Electrochemical impedance spectroscopy of $Bi_2Se_3$ thin films in 5 M $LiNO_3$: (**a**)—Nyquist plot for the SEI layer (−1.0 V ÷ 1.3 V vs. Ag/AgCl), (**b**)—Nyquist plot for the $Bi_2O_3$ layer (−1.0 V ÷ 0.5 V vs. Ag/AgCl), (**c**)—equivalent circuit scheme before cycling, (**d**)—equivalent circuit scheme during the cycling.

The resistance values of the electrochemical processes (Table 3) were calculated using the Levenberg–Marquardt algorithm [54].

**Table 3.** Cycle-dependent fitted resistance values of $Bi_2Se_3$ thin films with SEI and with the $Bi_2O_3$ layer.

| Layer | Resistance | Before Cycling | 1st | 5th | 10th | 25th | 50th | 100th |
|---|---|---|---|---|---|---|---|---|
| SEI | $R_{el}$, kΩ cm² | 0.5 | 0.9 | 2.3 | 2.8 | 2.9 | 3.0 | 3.1 |
| | $R_{layer}$, kΩ cm² | - | 2162 | 1515 | 772 | 252 | 208 | 225 |
| | $R_{ct}$, kΩ cm² | 584 | 154 | 379 | 275 | 1246 | 1965 | 490 |
| $Bi_2O_3$ | $R_{el}$, kΩ cm² | 0.1 | 0.4 | 0.8 | 1.3 | 1.4 | 1.7 | 2.0 |
| | $R_{layer}$, kΩ cm² | - | 112 | 130 | 170 | 196 | 39 | 26 |
| | $R_{ct}$, kΩ cm² | 111 | 13 | 10 | 17 | 25 | 17 | 20 |

The values of $R_{el}$ remained almost unchanged during the cycling, indicating good stability of the electrolyte over the whole 100 cycles for both samples. The $R_{el}$ values were 2.8 ± 0.3 kΩ cm² and 1.6 ± 0.3 kΩ cm² for the samples with the SEI layer and the $Bi_2O_3$

layer, respectively (Table 3). However, in the first five cycles, the $R_{el}$ values for both cases were significantly lower, which might be related to the pre-treatment processes of the $Bi_2Se_3$ thin films, including the stabilization of the surface layer which was also confirmed by the CV curves (Figure 2). For the sample with the SEI layer, $R_{el}$ was ~2 times higher than for the sample with the $Bi_2O_3$ layer, which might indicate that the processes occurring with the participation of the electrolyte are more complicated in the first case.

The semicircle at the medium-frequency range (Figure 9a,b) represents the charge-transfer resistance $R_{ct}$ of $Bi_2Se_3$ thin films. Starting from the first cycle, $R_{ct}$ values decreased ~4 times and ~9 times for the samples with SEI and $Bi_2O_3$ layers, respectively, which may be related to the beginning of textural and structural changes of the $Bi_2Se_3$ surface. After the 2nd cycle, the $R_{ct}$ for the sample with the $Bi_2O_3$ layer was almost constant ($17 \pm 5$ kΩ $cm^2$) until the 100th cycle, while, for the sample with the SEI layer, these values increased (from 154 kΩ $cm^2$ to 1965 kΩ $cm^2$). This might indicate the continuation of the textural and structural changes of the $Bi_2Se_3$ thin films with the formed SEI layer. The ~4 times decrease of $R_{ct}$ after the 100th cycle most likely corresponds to the electrochemical and mechanical degradation of the electrode.

For the samples with the SEI layer, the $R_{ct}$ was ~10–50 times higher than for the samples with the $Bi_2O_3$ layer, which might be related to the different structures of the SEI and $Bi_2O_3$ layers.

From the 1st to the 100th cycle, a small semicircle corresponding to $R_{layer}$ was observed in the low-frequency range (Figure 9a,b). For the sample with the formed SEI layer, $R_{layer}$ gradually decreased ~10 times from the 1st to the 100th cycle, probably indicating the mechanical and electrochemical degradation of the SEI layer by becoming more porous with cracks and cavities on the electrode surface [55,56].

For the samples with the $Bi_2O_3$ layer, the $R_{layer}$ gradually increased from the 1st to the 25th cycle. This represents the gradual formation of the $Bi_2O_3$ layer, including the pre-treatment processes (stabilization of the $Bi_2O_3$ layer) till the 9th cycle (Figure 2) and possible increase of the thickness of the $Bi_2O_3$ layer between the 10th and 25th cycles. After the 25th cycle, the $R_{layer}$ of the sample with the $Bi_2O_3$ layer started to gradually decrease from 196 kΩ $cm^2$ (25th cycle) to 39 kΩ $cm^2$ (50th cycle), which might be related to the degradation (formation of mechanical cracks and cavities) of the $Bi_2O_3$ layer. The comparison between the SEI and the $Bi_2O_3$ layers showed that $R_{layer}$ was ~5–20 times higher for the sample with the SEI layer. This probably indicates a higher affinity of energy for an electron of the $Bi_2O_3$ layer in comparison with the SEI layer.

### *3.3. Electrochemical Performance of $Bi_2Se_3$ Thin Films*

To investigate the possibility of using $Bi_2Se_3$ thin films as anodes in the ARLIBs systems, the charge/discharge capacity changes during the cycling were evaluated. After the first cycle, the initial charge and discharge capacities of the $Bi_2Se_3$ thin film in the samples with the SEI layer were 985 mAh $g^{-1}$ and 404 mAh $g^{-1}$ (Figure 10a). For the samples with the $Bi_2O_3$ layer, these capacities were lower at 250 mAh $g^{-1}$ (charge) and 115 mAh $g^{-1}$ (discharge), confirming that the formation of $Bi_2O_3$ makes the electrode less efficient in comparison with the samples covered by the SEI layer consisting of $Li_2O$ and $Li_2CO_3$ (Figure 9c). During the first 30 cycles, the charge/discharge capacities of the samples with the SEI layer decreased by ~3 times, which might be associated with the gradual degradation of the SEI layer, as $Li_2O$ and $Li_2CO_3$ are soluble in aqueous electrolyte compounds. Re-formation of the SEI layer might become more difficult due to the significant consumption of the dissolved $O_2$ and $CO_2$ during the first cycle of the SEI layer formation. For the sample with a $Bi_2O_3$ layer, the capacity increase (till the 10th cycle) and decrease (till the 30th cycle) were observed (Figure 10c), possibly indicating the gradual formation and degradation (the formation of mechanical cracks and cavities) of the $Bi_2O_3$ layer. Such tendencies of the re-formation of the SEI and $Bi_2O_3$ layers were also confirmed by the increment and decrement of the $R_{layer}$ values (Table 3). With the further cycling, the discharge capacities of the samples with the SEI layer also continued to decline,

but not as rapidly (~2 times) as in the previous 30 cycles, from 151 mAh $g^{-1}$ (30th cycle) to 79 mAh $g^{-1}$ (100th cycle). For the samples with the $Bi_2O_3$ layer, the values of both charge and discharge capacities remained constant after the 30th cycle and up to the 100th cycle. The initial Coulombic efficiency for the samples with the SEI layer was 41%. However, after cycling up to the 30th cycle, it increased up to 67% and remained almost constant up to the 100th cycle (73%) (Figure 10b). For the samples with the $Bi_2O_3$ layer, the Coulombic efficiency was almost constant until the 97th cycle (~40%) and decreased down to 33% during the next three cycles (Figure 10d).

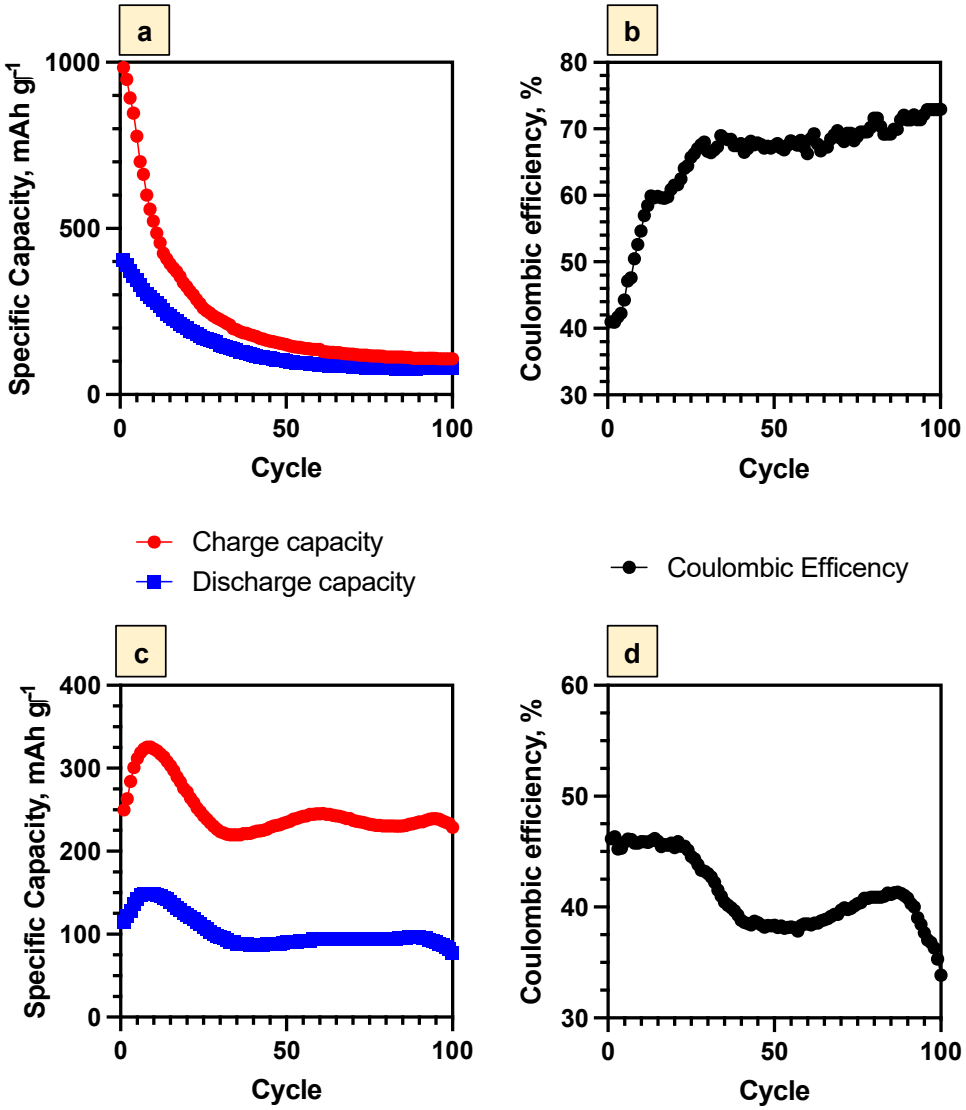


**Figure 10.** Galvanostatic charge/discharge cycling performances of $Bi_2Se_3$ thin films in 5M $LiNO_3$ at 1 C: (**a**)—cycling performance for the SEI layer (−1.0 V ÷ 1.3 V), (**b**)—Coulombic efficiency for the SEI layer (−1.0 V ÷ 1.3 V), (**c**)—cycling performance for the $Bi_2O_3$ layer (−1.0 V ÷ 0.5 V), (**d**)—Coulombic efficiency for the $Bi_2O_3$ layer (−1.0 V ÷ 0.5 V).

The comparison of the discharge capacities of the $Bi_2Se_3$ thin films with different previously reported anodes ($TiO_2$, $TiP_2O_7$, $L_{0.3}V_2O_5$, $L_{1.2}V_3O_8$) in the lithium aqueous electrolytes studied in this work (Table 4) show that the $Bi_2Se_3$ thin films with SEI and $Bi_2O_3$ layers demonstrate the highest specific capacities at the fastest charge/discharge rate (1 C), indicating their perspective application as anode electrodes in ARLIBs.

**Table 4.** Comparison of galvanostatic discharge cycling performances of different anodes in lithium aqueous electrolyte.

| Electrode | Electrolyte | C-rate | Initial Specific Capacity | Cycles | Specific Capacity | Capacity Retention | Coulombic Efficiency | Reference |
|---|---|---|---|---|---|---|---|---|
| $Bi_2Se_3$ thin film (SEI layer) | 5 M $LiNO_3$ | 1 C | 404 mAh $g^{-1}$ | 30 | 151 mAh $g^{-1}$ | 40% | 70% | This study |
| $Bi_2Se_3$ thin film ($Bi_2O_3$ layer) | 5 M $LiNO_3$ | 1 C | 115 mAh $g^{-1}$ | 30 | 96 mAh $g^{-1}$ | 83% | 43% | This study |
| $TiO_2$ | 21 M LiTFSI | 0.2 C | 115 mAh $g^{-1}$ | 40 | 8 mAh $g^{-1}$ | 7% | 70% | [24] |
| $TiP_2O_7$ | 5 M $LiNO_3$ | 0.1 C | 42 mAh $g^{-1}$ | 25 | 15 mAh $g^{-1}$ | 35% | - | [11] |
| $Li_{0.3}V_2O_5$ | 5 M $LiNO_3$ | 1 C | 75 mAh $g^{-1}$ | 50 | 38 mAh $g^{-1}$ | 51% | 99% | [50] |
| $Li_{1.2}V_3O_8$ | 1 M $Li_2SO_4$ | 1 C | 101 mAh $g^{-1}$ | 30 | 70 mAh $g^{-1}$ | 70% | - | [9] |

## 4. Conclusions

$Bi_2Se_3$ thin films were synthesized and investigated for their application in ARLIBs in aqueous the 5 M $LiNO_3$ electrolyte in two potential ranges which enabled two different interface layers, (−1.0 V ÷ 1.3 V—for $Li_2O$ and $Li_2CO_3$ SEI) and (−1.0 V ÷ 0.5 V—for $Bi_2O_3$). With the formed SEI layer, $Bi_2Se_3$ thin films demonstrated rapid pre-treatment (formation of stable SEI layer), high reversibility, and high transportation of $Li^+$ during the intercalation/deintercalation processes. For both SEI and $Bi_2O_3$ layers, the capacitive process dominated (>50%) $Li^+$ intercalation/deintercalation, which indicates the removal of limitations on charge transfer processes. In addition, the SEI layer enabled an $Li^+$ diffusion coefficient an order of magnitude higher than the $Bi_2O_3$ layer, which was in line or higher than that reported in the literature. The EIS investigation showed relatively stable and similar electrochemical performances for both the SEI and $Bi_2O_3$ layers up to the 100th cycle for electrolyte ($R_{el}$), while charge transfer ($R_{ct}$) and layer ($R_{layer}$) resistances changed during the cycling and were significantly lower for the $Bi_2O_3$. This may be attributed to the different structures and electron affinities of the SEI and the $Bi_2O_3$ layers.

The galvanostatic charge/discharge curves obtained at an intensive rate of 1 C for 100 cycles demonstrated that the formation of the SEI layer in the first cycle plays a crucial role in the electrode stabilization, which in turn, ensures high Coulombic efficiency (73%), high charge/discharge capacity, and protection from the mechanical and electrochemical degradation up to 100 cycles. Overall, the $Bi_2Se_3$ thin films with a formed SEI layer demonstrated better electrochemical performance in comparison to the ones with a formed $Bi_2O_3$ layer. These results demonstrate that the $Bi_2Se_3$ thin films can be promising candidates for use as anode materials for ARLIBs; however, further research is needed to optimize the electrochemical properties (e.g., capacity fading) of the system.

**Supplementary Materials:** The following supporting information can be downloaded at: https://www.mdpi.com/article/10.3390/batteries8100144/s1, Figure S1: Laboratory-made 3-electrode electrochemical cell system; Figure S2: As-synthesized $Bi_2Se_3$ thin film on the glass substrate: a—SEM image, b—EDX spectrum.

**Author Contributions:** Conceptualization, V.L., Y.R. and R.M.; methodology, V.L., Y.R., R.M., J.A., V.V., A.K. and A.S.; data curation, V.L., Y.R. and R.M.; Investigation, V.L., Y.R., R.M., J.A., V.V., A.K. and A.S.; Writing – original draft, V.L., Y.R., and R.M.; Writing – review & editing, V.L., Y.R., R.M., J.A., A.S., A.V. and D.E.; Project administration, D.E.; Supervisor, A.V. and D.E. All authors have read and agreed to the published version of the manuscript.

**Funding:** This research was funded by the European Regional Development Fund Project (ERDF) No. 1.1.1.1/19/A/139. Y.R. acknowledges the support of post-doctoral ERDF project No. 1.1.1.2/VIAA/4/20/694. V.L. also acknowledges the support of "Strengthening of the capacity of doctoral studies at the Univer-

sity of Latvia within the framework of the new doctoral model", identification No. 8.2.2.0/20/I/006. A.S. acknowledges the support from the Institute of Solid State Physics, University of Latvia, which, as the Center of Excellence, has received funding from the European Union's Horizon 2020 Framework Programme H2020-WIDESPREAD-01-2016-2017-TeamingPhase2 under grant agreement No. 739508, project CAMART$^2$.

**Institutional Review Board Statement:** Not applicable.

**Informed Consent Statement:** Not applicable.

**Data Availability Statement:** The data presented in this study are available on request from the corresponding author. The data are not publicly available as they are part of ongoing research.

**Conflicts of Interest:** The authors declare no conflict of interest. The funders had no role in the design of the study; in the collection, analyses, or interpretation of data; in the writing of the manuscript, or in the decision to publish the results.

## References

1. Dunn, B.; Kamath, H.; Tarascon, J.M. Electrical energy storage for the grid: A battery of choices. *Science* **2011**, *334*, 928–935. [CrossRef] [PubMed]
2. Wang, X.; Hou, Y.; Zhu, Y.; Wu, Y.; Holze, R. An Aqueous Rechargeable Lithium Battery Using Coated Li Metal as Anode. *Sci. Rep.* **2013**, *3*, 4–8. [CrossRef]
3. Chen, T.; Jin, Y.; Lv, H.; Yang, A.; Liu, M.; Chen, B.; Xie, Y.; Chen, Q. Applications of Lithium-Ion Batteries in Grid-Scale Energy Storage Systems. *Trans. Tianjin Univ.* **2020**, *26*, 208–217. [CrossRef]
4. Yao, L.; Xu, S.; Tang, A.; Zhou, F.; Hou, J.; Xiao, Y.; Fu, Z. A review of lithium-ion battery state of health estimation and prediction methods. *World Electr. Veh. J.* **2021**, *12*, 113. [CrossRef]
5. Li, W.; Dahn, J.R.; Wainwright, D.S. Rechargeable Lithium Batteries with Aqueous Electrolytes. *Science* **1994**, *264*, 1115–1118. [CrossRef]
6. Alias, N.; Mohamad, A.A. Advances of aqueous rechargeable lithium-ion battery: A review. *J. Power Sources* **2015**, *274*, 237–251. [CrossRef]
7. Zhang, H.; Liu, X.; Li, H.; Hasa, I.; Passerini, S. Challenges and Strategies for High-Energy Aqueous Electrolyte Rechargeable Batteries. *Angew. Chem. Int. Ed.* **2021**, *60*, 598–616. [CrossRef] [PubMed]
8. Konarov, A.; Voronina, N.; Jo, J.H.; Bakenov, Z.; Sun, Y.K.; Myung, S.T. Present and Future Perspective on Electrode Materials for Rechargeable Zinc-Ion Batteries. *ACS Energy Lett.* **2018**, *3*, 2620–2640. [CrossRef]
9. Cheng, C.; Li, Z.H.; Zhan, X.Y.; Xiao, Q.Z.; Lei, G.T.; Zhou, X.D. A macaroni-like $Li_{1.2}V_3O_8$ nanomaterial with high capacity for aqueous rechargeable lithium batteries. *Electrochim. Acta* **2010**, *55*, 4627–4631. [CrossRef]
10. Xu, T.; Zhao, M.; Duan, W.; Ding, M.; Lashari, N.u.R.; Wang, F.; Song, X. Excellent Rate Performance and Cycling Stability of $TiP_2O_7$@C/Carbon Nanotubes for the Aqueous Rechargeable Lithium-Ion Battery. *Energy Technol.* **2019**, *7*, 1900534. [CrossRef]
11. Wang, H.; Huang, K.; Zeng, Y.; Yang, S.; Chen, L. Electrochemical properties of $TiP_2O_7$ and $LiTi_2(PO_4)_3$ as anode material for lithium ion battery with aqueous solution electrolyte. *Electrochim. Acta* **2007**, *52*, 3280–3285. [CrossRef]
12. Singh, R.; Kumari, P.; Kumar, M.; Ichikawa, T.; Jain, A. Implementation of Bismuth Chalcogenides as an Efficient Anode: A Journey from Conventional Liquid Electrolyte to an All-Solid-State Li-Ion Battery. *Molecules* **2020**, *25*, 3733. [CrossRef]
13. Wen, Y.; Liu, Y.; Bin, D.; Wang, Z.; Wang, C.; Cao, Y.; Ai, X.; Xia, Y. High performance $TiP_2O_7$ nanoporous microsphere as anode material for aqueous lithium-ion batteries. *Sci. China Chem.* **2019**, *62*, 118–125. [CrossRef]
14. Xie, L.; Yang, Z.; Sun, J.; Zhou, H.; Chi, X.; Chen, H.; Li, A.X.; Yao, Y.; Chen, S. $Bi_2Se_3$/C Nanocomposite as a New Sodium-Ion Battery Anode Material. *Nano-Micro Lett.* **2018**, *10*, 50. [CrossRef]
15. Ni, J.; Bi, X.; Jiang, Y.; Li, L.; Lu, J. Bismuth chalcogenide compounds $Bi_2X_3$ (X=O, S, Se): Applications in electrochemical energy storage. *Nano Energy* **2017**, *34*, 356–366. [CrossRef]
16. Liu, W.; Lukas, K.C.; McEnaney, K.; Lee, S.; Zhang, Q.; Opeil, C.P.; Chen, G.; Ren, Z. Studies on the $Bi_2Te_3$-$Bi_2Se_3$-$Bi_2S_3$ system for mid-temperature thermoelectric energy conversion. *Energy Environ. Sci.* **2013**, *6*, 552–560. [CrossRef]
17. Bludská, J.; Jakubec, I.; Karamazov, S.; Horák, J.; Uher, C. Lithium ions in the van der Waals gap of $Bi_2Se_3$ single crystals. *J. Solid State Chem.* **2010**, *183*, 2813–2817. [CrossRef]
18. Chen, X.; Tang, H.; Huang, Z.; Zhou, J.; Ren, X.; Huang, K.; Qi, X.; Zhong, J. Flexible Bismuth Selenide/Graphene composite paper for lithium-ion batteries. *Ceram. Int.* **2017**, *43*, 1437–1442. [CrossRef]
19. Han, G.; Chen, Z.G.; Ye, D.; Yang, L.; Wang, L.; Drennan, J.; Zou, J. In-doped $Bi_2Se_3$ hierarchical nanostructures as anode materials for Li-ion batteries. *J. Mater. Chem. A* **2014**, *2*, 7109–7116. [CrossRef]
20. Wang, G.J.; Zhang, H.P.; Fu, L.J.; Wang, B.; Wu, Y.P. Aqueous rechargeable lithium battery (ARLB) based on $LiV_3O_8$ and $LiMn_2O_4$ with good cycling performance. *Electrochem. Commun.* **2007**, *9*, 1873–1876. [CrossRef]
21. Wen, Y.; Chen, L.; Pang, Y.; Guo, Z.; Bin, D.; Wang, Y.g.; Wang, C.; Xia, Y. $TiP_2O_7$ and Expanded Graphite Nanocomposite as Anode Material for Aqueous Lithium-Ion Batteries. *ACS Appl. Mater. Interfaces* **2017**, *9*, 8075–8082. [CrossRef]
22. Xiong, H.; Dufek, E.J.; Gering, K.L. Batteries. *Comprehensive Energy Systems.* **2018**, *2*(5), 629–662. [CrossRef]

23. Karkera, G.; Prakash, A.S. An Inorganic Electrolyte Li–$O_2$ Battery with High Rate and Improved Performance. *ACS Appl. Energy Mater.* **2018**, *1*, 1381–1388. [CrossRef]
24. Subramanya, U.; Chua, C.; He Leong, V.G.; Robinson, R.; Cruz Cabiltes, G.A.; Singh, P.; Yip, B.; Bokare, A.; Erogbogbo, F.; Oh, D. Carbon-based artificial SEI layers for aqueous lithium-ion battery anodes. *RSC Adv.* **2019**, *10*, 674–681. [CrossRef]
25. Suo, L.; Oh, D.; Lin, Y.; Zhuo, Z.; Borodin, O.; Gao, T.; Wang, F.; Kushima, A.; Wang, Z.; Kim, H.C.; et al. How Solid-Electrolyte Interphase Forms in Aqueous Electrolytes. *J. Am. Chem. Soc.* **2017**, *139*, 18670–18680. [CrossRef]
26. Suo, L.; Borodin, O.; Gao, T.; Olguin, M.; Ho, J.; Fan, X.; Luo, C.; Wang, C.; Xu, K. "Water-in-salt" electrolyte enables high-voltage aqueous lithium-ion chemistries. *Science* **2015**, *350*, 938–943. [CrossRef]
27. Zhi, J.; Zehtab Yazdi, A.; Valappil, G.; Haime, J.; Chen, P. Artificial solid electrolyte interphase for aqueous lithium energy storage systems. *Sci. Adv.* **2017**, *3*, e1701010. [CrossRef]
28. Wessells, C.; Ruff, R.; Huggins, R.A.; Cui, Y. Investigations of the electrochemical stability of aqueous electrolytes for lithium battery applications. *Electrochem. Solid-State Lett.* **2010**, *13*, 2010–2013. [CrossRef]
29. Andzane, J.; Kunakova, G.; Charpentier, S.; Hrkac, V.; Kienle, L.; Baitimirova, M.; Bauch, T.; Lombardi, F.; Erts, D. Catalyst-free vapour–solid technique for deposition of $Bi_2Te_3$ and $Bi_2Se_3$ nanowires/nanobelts with topological insulator properties. *Nanoscale* **2015**, *7*, 15935–15944. [CrossRef]
30. Andzane, J.; Felsharuk, A.; Sarakovskis, A.; Malinovskis, U.; Kauranens, E.; Bechelany, M.; Niherysh, K.A.; Komissarov, I.V.; Erts, D. Thickness-dependent properties of ultrathin bismuth and antimony chalcogenide films formed by physical vapor deposition and their application in thermoelectric generators. *Mater. Today Energy* **2021**, *19*, 100587. [CrossRef]
31. Meija, R.; Lazarenko, V.; Skrastina, A.; Rublova, Y.; Andzane, J.; Voikiva, V.; Viksna, A.; Erts, D. The Electrochemical Characterization of Nanostructured $Bi_2Se_3$ Thin Films in an Aqueous Na Electrolyte. *Batteries* **2022**, *8*, 25. [CrossRef]
32. Baitimirova, M.; Andzane, J.; Petersons, G.; Meija, R.; Poplausks, R.; Romanova, M.; Erts, D. Vapor–solid synthesis and enhanced thermoelectric properties of non-planar bismuth selenide nanoplates on graphene substrate. *J. Mater. Sci.* **2016**, *51*, 8224–8232. [CrossRef]
33. Andzane, J.; Buks, K.; Strakova, M.N.; Zubkins, M.; Bechelany, M.; Marnauza, M.; Baitimirova, M.; Erts, D. Structure and Doping Determined Thermoelectric Properties of $Bi_2Se_3$ Thin Films Deposited by Vapour-Solid Technique. *IEEE Trans. Nanotechnol.* **2019**, *18*, 948–954. [CrossRef]
34. Erts, D.; Katkevics, J.; Sjomkane, M.; Andzane, J.; Sarakovskis, A.; Smits, K.; Viksna, A.; Rublova, Y.; Meija, R. EIS characterization of aging and humidity-related behavior of $Bi_2Se_3$ films of different morphologies. *Nano-Struct. Nano-Objects* **2022**, *30*, 100847. [CrossRef]
35. Kumari, P.; Singh, R.; Awasthi, K.; Ichikawa, T.; Kumar, M.; Jain, A. Highly stable nanostructured $Bi_2Se_3$ anode material for all solid-state lithium-ion batteries. *J. Alloys Compd.* **2020**, *838*, 155403. [CrossRef]
36. Li, W.; Yao, H.; Yan, K.; Zheng, G.; Liang, Z.; Chiang, Y.M.; Cui, Y. The synergetic effect of lithium polysulfide and lithium nitrate to prevent lithium dendrite growth. *Nat. Commun.* **2015**, *6*, 7436. [CrossRef]
37. Xin, X.; Ito, K.; Dutta, A.; Kubo, Y. Dendrite-Free Epitaxial Growth of Lithium Metal during Charging in Li–$O_2$ Batteries. *Angew. Chem.* **2018**, *130*, 13390–13394. [CrossRef]
38. Ahmad, Z.; Venturi, V.; Hafiz, H.; Viswanathan, V. Interfaces in Solid Electrolyte Interphase: Implications for Lithium-Ion Batteries. *J. Phys. Chem. C* **2021**, *125*, 11301–11309. [CrossRef]
39. Kitz, P.G.; Novák, P.; Berg, E.J. Influence of Water Contamination on the SEI Formation in Li-Ion Cells: An Operando EQCM-D Study. *ACS Appl. Mater. Interfaces* **2020**, *12*, 15934–15942. [CrossRef]
40. Chen, S.; Fang, Y.M.; Li, J.; Sun, J.J.; Chen, G.N.; Yang, H.H. Study on the electrochemical catalytic properties of the topological insulator $Bi_2Se_3$. *Biosens. Bioelectron.* **2013**, *46*, 171–174. [CrossRef]
41. Chaolong, Y. *Electrochemical Study of Bismuth Chalcogenides*; H.H. Wills Physics laboratory University of Bristol: Bristol, UK, 2021.
42. An, S.J.; Li, J.; Daniel, C.; Mohanty, D.; Nagpure, S.; Wood, D.L. The state of understanding of the lithium-ion-battery graphite solid electrolyte interphase (SEI) and its relationship to formation cycling. *Carbon* **2016**, *105*, 52–76. [CrossRef]
43. Lv, P.; Zhao, H.; Zeng, Z.; Gao, C.; Liu, X.; Zhang, T. Self-assembled three-dimensional hierarchical NiO nano/microspheres as high-performance anode material for lithium ion batteries. *Appl. Surf. Sci.* **2015**, *329*, 301–305. [CrossRef]
44. Meng, A.; Yuan, X.; Shen, T.; Li, Z.; Jiang, Q.; Xue, H.; Lin, Y.; Zhao, J. One-step synthesis of flower-like $Bi_2O_3/Bi_2Se_3$ nanoarchitectures and $NiCoSe_2/Ni_{0.85}Se$ nanoparticles with appealing rate capability for the construction of high-energy and long-cycle-life asymmetric aqueous batteries. *J. Mater. Chem. A* **2019**, *7*, 17613–17625. [CrossRef]
45. Chen, Z.; Liu, T.; Zhao, Z.; Zhang, Z.; Han, X.; Han, P.; Li, J.; Wang, J.; Li, J.; Huang, S.; et al. Fast anion intercalation into graphite cathode enabling high-rate rechargeable zinc batteries. *J. Power Sources* **2020**, *457*, 227994. [CrossRef]
46. Deng, X.; Wei, Z.; Cui, C.; Liu, Q.; Wang, C.; Ma, J. Oxygen-deficient anatase $TiO_2$@C nanospindles with pseudocapacitive contribution for enhancing lithium storage. *J. Mater. Chem. A* **2018**, *6*, 4013–4022. [CrossRef]
47. Xiong, T.; Wang, Y.; Yin, B.; Shi, W.; Lee, W.S.V.; Xue, J. Bi2S3 for Aqueous Zn Ion Battery with Enhanced Cycle Stability. *Nano-Micro Lett.* **2020**, *12*, 8. [CrossRef]
48. Luo, L.; Song, J.; Song, L.; Zhang, H.; Bi, Y.; Liu, L.; Yin, L.; Wang, F.; Wang, G. Flexible Conductive Anodes Based on 3D Hierarchical Sn/NS-CNFs@rGO Network for Sodium-Ion Batteries. *Nano-Micro Lett.* **2019**, *11*, 63. [CrossRef]
49. Kim, T.; Choi, W.; Shin, H.C.; Choi, J.Y.; Kim, J.M.; Park, M.S.; Yoon, W.S. Applications of voltammetry in lithium ion battery research. *J. Electrochem. Sci. Technol.* **2020**, *11*, 14–25. [CrossRef]

50. Bao, J.; Zhou, M.; Zeng, Y.; Bai, L.; Zhang, X.; Xu, K.; Xie, Y. $Li_{0.3}V_2O_5$ with high lithium diffusion rate: A promising anode material for aqueous lithium-ion batteries with superior rate performance. *J. Mater. Chem. A* **2013**, *1*, 5423–5429. [CrossRef]
51. Wu, W.; Shanbhag, S.; Wise, A.; Chang, J.; Rutt, A.; Whitacre, J.F. High Performance $TiP_2O_7$ Based Intercalation Negative lectrode for Aqueous Lithium-Ion Batteries via a Facile Synthetic Route. *J. Electrochem. Soc.* **2015**, *162*, A1921–A1926. [CrossRef]
52. Lee, Y.S.; Ryu, K.S. Study of the lithium diffusion properties and high rate performance of $TiNb_6O_{17}$ as an anode in lithium secondary battery. *Sci. Rep.* **2017**, *7*, 16617. [CrossRef]
53. Abe, Y.; Hori, N.; Kumagai, S. Electrochemical impedance spectroscopy on the performance degradation of $LiFePO_4$/graphite lithium-ion battery due to charge-discharge cycling under different c-rates. *Energies* **2019**, *12*, 4507. [CrossRef]
54. Moré, J.J. *The Levenberg-Marquardt Algorithm: Implementation and Theory*; Springer: Berlin/Heidelberg, Germany, 1978; pp. 105–116. [CrossRef]
55. Deshpande, R.D.; Bernardi, D.M. Modeling Solid-Electrolyte Interphase (SEI) Fracture: Coupled Mechanical/Chemical Degradation of the Lithium Ion Battery. *J. Electrochem. Soc.* **2017**, *164*, A461–A474. [CrossRef]
56. Bhattacharya, S.; Riahi, A.R.; Alpas, A.T. Electrochemical cycling behaviour of lithium carbonate ($Li_2CO_3$) pre-treated graphite anodes—SEI formation and graphite damage mechanisms. *Carbon* **2014**, *77*, 99–112. [CrossRef]